

## RESEARCH ARTICLE

10.1002/2014JB011323

## Key Points:

- Thermal front propagation is controlled by the dimensionless parameter  $Q_D$
- The induced seismicity is conditioned by thermal front propagation
- The timing of seismicity due to the thermal effect could be predicted

## Supporting Information:

- Readme
- Dataset S1

## Correspondence to:

Q. Gan,  
gqx5004@psu.edu

## Citation:

Gan, Q., and D. Elsworth (2014), Thermal drawdown and late-stage seismic-slip fault reactivation in enhanced geothermal reservoirs, *J. Geophys. Res. Solid Earth*, 119, 8936–8949, doi:10.1002/2014JB011323.

Received 28 MAY 2014

Accepted 4 NOV 2014

Accepted article online 7 NOV 2014

Published online 11 DEC 2014

## Thermal drawdown and late-stage seismic-slip fault reactivation in enhanced geothermal reservoirs

Quan Gan<sup>1</sup> and Derek Elsworth<sup>1</sup>

<sup>1</sup>Department of Energy and Mineral Engineering, EMS Energy Institute and G3 Center, Pennsylvania State University, University Park, Pennsylvania, USA

**Abstract** Late-stage seismic slip in geothermal reservoirs has been shown as a potential mechanism for inducing seismic events of magnitudes to  $\sim 2.6$  as late as two decades into production. We investigate the propagation of fluid pressures and thermal stresses in a prototypical geothermal reservoir containing a centrally located critically stressed fault from a doublet injector and withdrawal well to define the likelihood, timing, and magnitude of events triggered by both fluid pressures and thermal stresses. We define two bounding modes of fluid production from the reservoir. For injection at a given temperature, these bounding modes relate to either low- or high-relative flow rates. At low relative dimensionless flow rates the pressure pulse travels slowly, the pressure-driven changes in effective stress are muted, but thermal drawdown propagates through the reservoir as a distinct front. This results in the lowest likelihood of pressure-triggered events but the largest likelihood of late-stage thermally triggered events. Conversely, at high relative non-dimensional flow rates the propagating pressure pulse is larger and migrates more quickly through the reservoir but the thermal drawdown is uniform across the reservoir and without the presence of a distinct thermal front, and less capable of triggering late-stage seismicity. We evaluate the uniformity of thermal drawdown as a function of a dimensionless flow rate  $Q_D$  that scales with fracture spacing  $s$  (m), injection rate  $q$  (kg/s), and the distance between the injector and the target point  $L^*$  ( $Q_D \propto qs^2/L^*$ ). This parameter enables the reservoir characteristics to be connected with the thermal drawdown response around the fault and from that the corresponding magnitude and timing of seismicity to be determined. These results illustrate that the dimensionless temperature gradient adjacent to the fault  $dT_D/dx_D$  is exclusively controlled by the factor  $Q_D$ . More significantly, this temperature gradient correlates directly with both the likelihood and severity of triggered events, enabling the direct scaling of likely magnitudes and timing to be determined a priori and directly related to the characteristics of the reservoir. This dimensionless scaling facilitates design for an optimum  $Q_D$  value to yield both significant heat recovery and longevity of geothermal reservoirs while minimizing associated induced seismicity.

### 1. Introduction

Harvesting geothermal energy from deep fractured low-permeability formations has become a feasible method to ease the demand on fossil energy. Predicting mass rates and temperatures of fluid production and assessing induced seismicity are intimately connected topics that require an intimate and complete understanding of subsurface coupled THMC (Thermal-Hydrological-Mechanical-Chemical) processes [Taron and Elsworth, 2010]. The associated thermal drawdown response of the rock mass results from the circulation of a heat-transfer fluid [Bodvarsson, 1969; B dvarsson and Tsang, 1982]. Thermal drawdown in the fractured porous medium may be determined by accommodating the essential components of the reservoir—heat transfer from the reservoir matrix to the fluid by conduction and then advection across the reservoir—for which a variety of analytical approaches are available [Elsworth, 1989a, 1989b, 1990; Ganguly and Mohan Kumar, 2014; Gringarten and Witherspoon, 1973; Gringarten et al., 1975; Pruess, 1983; Pruess and Wu, 1993; Ghassemi et al., 2003]. These approaches are based on the assumptions of locally 1-D heat conduction in an infinite medium, and that the fluid flow in the fractured medium instantaneously reaches local thermal equilibrium [Shaik et al., 2011].

To accommodate more general flow geometries, including the inclusion of heterogeneity, a variety of numerical methods are available to represent response. Such models also accommodate key process of heat transfer in the subsurface in accommodating dual porosity to describe heat exchange between the porous fracture and the low porosity rock [Xu et al., 2003; Xu et al., 2004, 2001; Elsworth, 1989a, 1989b; Elsworth and Xiang, 1989]. The principal heat transfer processes include first heat conduction between the

matrix and fluid within the fractures then the advection of that heat across and then out from the reservoir. Depending on the fluid velocity in the fracture, the temperature gradient between the circulating fluid and the adjacent rock varies significantly. In general, the amount of heat energy transferred from the rock is controlled by the heat transfer area, the temperature difference between rock and fluid, and the velocity of the circulating fluid [Holman, 2002].

In addition to exploring thermal drawdown in the reservoir, and its influence on effluent fluid temperatures, the spatial distribution of reservoir temperature is also influenced by rates of fluid circulation. This thermal drawdown of the rock is also capable of inducing thermal stresses, which in turn are implicated in the potential for induced seismicity and increase the likelihood of late stage fault reactivation [Gan and Elsworth, 2014]. The role of thermal stresses in reservoirs has been explored with respect to the evolution of permeability [Elsworth, 1989a, 1989b] and of stresses [Segall and Fitzgerald, 1998]. Thermally driven stress changes in geothermal reservoirs are known to be potentially significant. In this work we specifically explore rates of stress generation and their propagation through the reservoir as controlled by thermal capacitance of a dual porosity system, and ultimately on the potential to develop unstable slip. In this, the induced thermal stresses cause the unloading of the fault by reducing maximum in situ stress, thereby reducing shear strength and therefore enabling slip reactivation as a potentially seismic event. The severity of the reactivation event appears directly related to the spatial gradient of rock temperature that develops in the reservoir [Gan and Elsworth, 2014]—a uniform reduction in temperature will have a muted change in thermal stresses. Hence, in this work we explore the impact of fluid circulation rates on the heterogeneity of thermal drawdown that may develop within the reservoir and its potential impact on the timing and magnitude of induced seismicity.

The following develops a dimensionless semi-analytical model which incorporates the reservoir scale, fracture spacing and injection mass flow rate to determine thresholds for the evolution of uniform or shock-front distributions of thermal drawdown within the rock comprising the reservoir. The semi-analytical model is derived based on the balance of heat conduction within the fractured medium and the Warren-Root fracture model. Key variables are prescribed that may then be used to assess the propagation of stress fronts through the reservoir and from that define the likelihood, timing, and magnitude of late stage events that might occur on reactivated faults.

## 2. Mathematical Formulation

To assess and elucidate the fundamental heat transfer processes within the fractured-porous medium, a basic model is presented in Figure 1 for the following analytical study. The two-dimensional reservoir is characterized by an orthogonal fracture network with uniform fracture spacing  $s$  (m) in both  $x$  and  $z$  directions and with a uniform fracture aperture  $b$  (m). The fractures are the sole conduits for fluid circulation within the reservoir. This parallel fracture model (PFM) has been validated to effectively characterize heat recovery from an arrangement of prismatic blocks, which are thermally isolated from the geologic host medium [Elsworth, 1990]. Here we relax the restrictions imposed by prior analytical solutions by imposing the following assumptions:

1. The initial temperature of the reservoir and interstitial fluid is uniform at  $T_0$  with cold water injected at constant rate and at constant temperature  $T_{inj}$ .
2. Heat conduction occurs primarily in  $z$  directions along the fractures with thermal conductivity  $K_r$  and with heat transfer in the vertical direction neglected. We assume that the majority of heat transfer occurs normal to the direction from injection well to production well. There is no heat transfer by radiation within the fractures. The diffusion of heat in the rock matrix occurs only in the direction orthogonal to the fracture plane.
3. The density and heat capacity for both the rock and fluid are constant. Also the thermal conductivity of the rock matrix is assumed constant.

The differential equations governing heat transfer in the fracture are based on the balance of heat energy in the control volume of fractures, defined as

$$\rho_w c_w \frac{\partial T_w(x, t)}{\partial t} = -v \rho_w c_w \frac{\partial T_w(x, t)}{\partial x} + \frac{2K_r}{b} \frac{\partial T_r(x, z, t)}{\partial z} \Big|_{z=b/2} \quad (1)$$

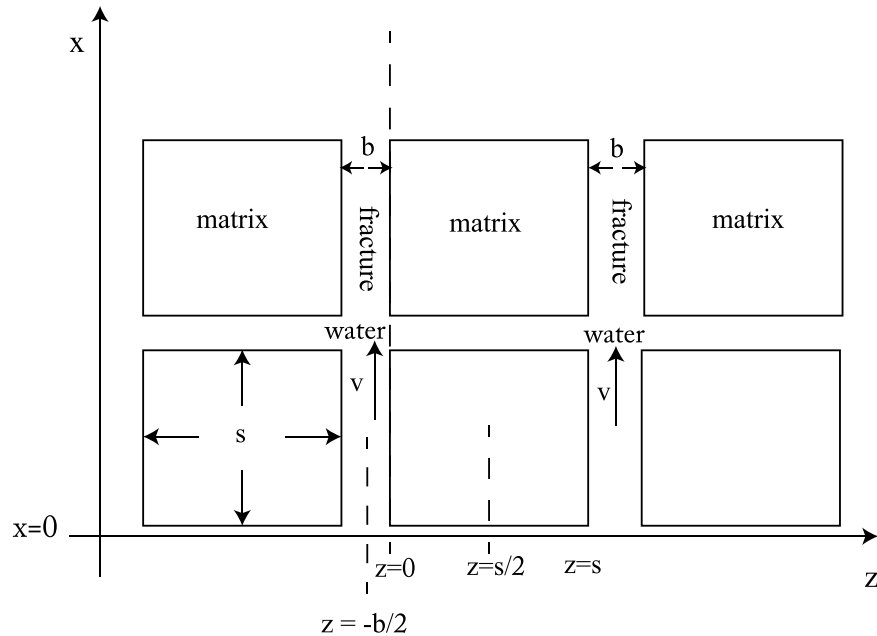


**Figure 1.** Schematic of analytical heat conduction within fractured medium. The identical fractures with aperture  $b$  are equally separated at the spacing  $s$ .

where  $v$  is the fluid velocity (m/s),  $T_w(x, t)$  is the temperature of water,  $T_m(x, z, t)$  is the temperature of the rock matrix,  $b$  is the fracture aperture (m),  $c_w$  is the heat capacity of water (J/kg/°C),  $\rho_w$  is the density of water, and  $K_r$  is the thermal conductivity of the rock (J/s/m/°C).

The temperature of the rock matrix is governed by the one-dimensional heat conduction equation:

$$\frac{\partial^2 T_r(x, z, t)}{\partial z^2} = \frac{\rho_r c_r}{K_r} \frac{\partial T_r(x, z, t)}{\partial t} \tag{2}$$

where  $\rho_r$  is the density of the rock matrix, and  $c_r$  is the heat capacity of the rock.

The thermal drawdown response may be determined under a variety of different reservoir configurations by using a unified dimensionless analytical model. We redefine the governing equations in terms of the non-dimensional variables of dimensionless flow rate,  $Q_D$ , mean temperatures of the rock,  $T_{Dr}$ , and water,  $T_{Dw}$ , time,  $t_D$ , and length scales,  $x_D$  and  $z_D$ , as,

$$Q_D = \frac{\rho_w c_w}{K_r} \left( \frac{q_1}{L^*} \right) s \tag{3}$$

$$q_1 = \frac{q}{\rho_w \frac{W}{s} H} = \frac{qs}{\rho_w HW} \tag{4}$$

where  $q$  is the injection rate (kg/s),  $q_1$  is the volumetric flow rate per fracture per unit thickness ( $m^2/s$ ), the terms  $H$  and  $W$  are the height and width of the reservoir, respectively, and  $L^*$  is the distance between the injector and the target point. Substituting equation (4) into equation (3) defines the dimensionless flow rate as,

$$Q_D = \frac{qs^2 c_w}{K_r HL^* W} \tag{5}$$

Dimensionless time  $t_D$  is defined as,

$$t_D = \frac{\rho_w c_w}{K_r} \frac{\rho_w c_w}{\rho_r c_r} \left( \frac{q_1}{L^*} \right)^2 t = \frac{t}{K_r \rho_r c_r} \left( \frac{qs c_w}{HWL^*} \right)^2 \tag{6}$$

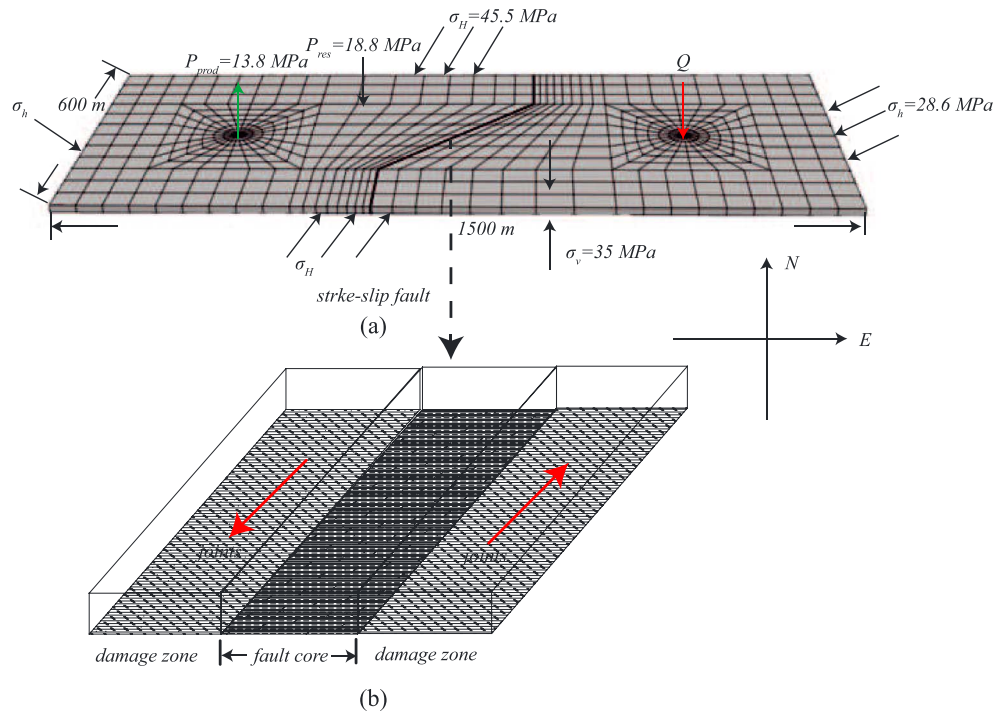


**Figure 2.** (a) Model geometry and applied stress boundary condition, initial condition; (b) strike-slip fault geometry in model.

The dimensionless rock temperature  $T_{Dr}$  is defined as,

$$T_{Dr} = \frac{T_{inj} - T_r}{T_{inj} - T_0} \quad (7)$$

The dimensionless outlet water temperature  $T_{Dw}$  is defined as,

$$T_{Dw} = \frac{T_{inj} - T_w}{T_{inj} - T_0} \quad (8)$$

The dimensionless length scales  $x_D$  and  $z_D$  are defined separately as,

$$x_D = \frac{x}{L^*} \quad (9)$$

$$z_D = \frac{z}{s} \quad (10)$$

$$\eta_w = \frac{L^* K_r}{v \rho_w c_w s b} = \frac{1}{Q_D} \quad (11)$$

These defined non-dimensional parameters,  $Q_D$ ,  $t_D$ ,  $T_{Dr}$ , and  $T_{Dw}$  length scales  $x_D$ ,  $z_D$ , and  $\eta_w$  are used to transform and simplify the governing equations. By assuming that heat storage term in the fracture is negligible, the corresponding dimensional governing equations of (1) and (2) could be represented in dimensionless form as,

$$\frac{\partial T_{Dw}(x, t)}{\partial x_D} = 2\eta_w \frac{\partial T_{Dr}(x, z, t)}{\partial z_D} \Big|_{z=b/2} \quad (12)$$

$$\frac{\partial^2 T_{Dr}(x, z, t)}{\partial z_D^2} = \eta_w^2 \frac{\partial T_{Dr}(x, z, t)}{\partial t_D} \quad (13)$$

### 3. Model Description

This present work is a continuation of prior characterizations that define the potential for late-stage fault reactivation in geothermal reservoirs [Gan and Elsworth, 2014]. This extension is to codify the likelihood, timing, and magnitude of potential events as a function of fracture geometry and fluid transmission characteristics and applied flow rates. The heat transfer problem is approached using semi-analytical and

**Table 1.** Material Properties Input in the Model for Host Rock and Fault [Gan and Elsworth, 2014]

Parameters	In-tact Rock	Damage Zone	Core Zone
Young's modulus (GPa)	8	1.5	1.5
Shear modulus (GPa)	5.5	1	1
Permeability (m <sup>2</sup> )	1 × 10 <sup>-16</sup>	5 × 10 <sup>-13</sup>	1 × 10 <sup>-17</sup>
Poisson's ratio	0.2	0.2	0.2
Friction angle	30	30	30
Fracture porosity	0.8	0.8	0.8
Fracture permeability (m <sup>2</sup> )	1 × 10 <sup>-13</sup>	5 × 10 <sup>-13</sup>	1 × 10 <sup>-17</sup>
Cohesion (MPa)	8	0	0
Tensile strength (MPa)	10	0	0

numerical methods, and this then applied to define the propagation of stress fronts and their impact on seismicity. Calculations are completed using a numerical simulator that couples the analysis of mass and energy transport in porous fractured media (TOUGH) with mechanical deformation (FLAC3D) [Taron and Elsworth, 2009, 2010; Xu et al., 2004]. These analyses are completed using the non-dimensional parameters noted in equation (5) through (8).

The reservoir geometry includes a 2-D rectangular (1500 m × 600 m × 15 m) reservoir containing three sets of orthogonal fractures (see the mesh in Figure 2). A strike-slip fault is located in the center of reservoir flanked by equidistant injection and withdrawal wells. The initial distribution of reservoir temperature is uniform with an initial rock and fluid temperature of 250 °C, an initial reservoir pressure of 18.8 MPa, and with cold water injected under constant mass flow rate with a constant enthalpy of 2.0 × 10<sup>5</sup> J/kg (equivalent to 43 °C) and with the production well operated under a constant pressure of 13.8 MPa. A minimum in situ stress of 28.8 MPa is imposed in the W-E direction, and the maximum horizontal stress of 45 MPa is applied in the N-S direction. The model boundaries are set as no-flow boundaries with applied constant stresses.

The inserted strike-slip fault is finely discretized to represent the anticipated mechanical and transport characteristics of a fault with a low permeability core (thickness 0.8 m) flanked by higher permeability damage zones (thickness 1.2 m). The fault acts as flow conduit along its axis but as a barrier/impediment for the propagation of the fluid front from the injection to the recovery well. A ubiquitous-joint constitutive model is applied to represent the elastic-plastic behavior of the fault. The fractures comprising the fracture network and host rock have the same initial angle of internal friction of 30° (see Table 1) [Biot, 1941; Byerlee, 1978]. The friction angle of the fault joint is 30°. We adopt a linear strain-softening relationship that implies that the friction angle decreases with an increase in the plastic strain.

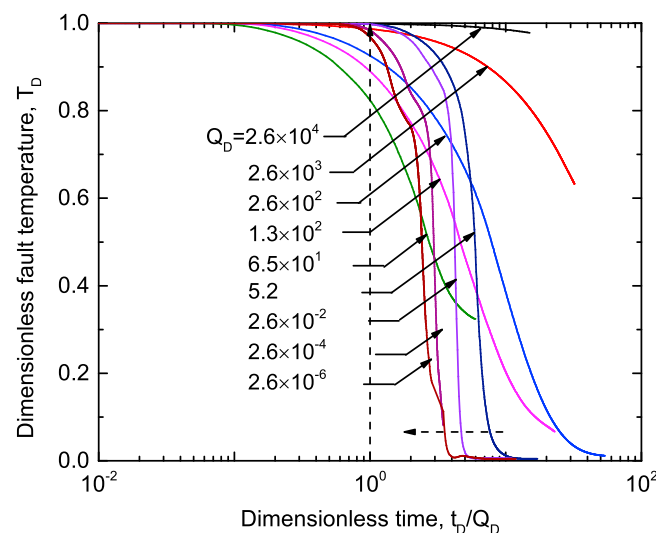


**Figure 3.** Dimensionless fault temperature  $T_D$  evolution vs dimensionless time  $t_D/Q_D$  under  $Q_D$  values varies, respectively, from  $2.6 \times 10^{-6}$  to  $2.6 \times 10^4$ .

Fluid and heat transport is accommodated by representing the reservoir as an equivalent dual permeability continuum. This dual porosity model accommodates the local thermal disequilibrium in heat exchange between rock matrix and fluid in fractures. The dual permeability continuum is represented by orthogonal fracture sets spaced equally in the three principal directions and with uniform initial aperture and with a functionally impermeable matrix.

#### 4. Thermal Drawdown Behavior

Since the thermal stresses that are induced adjacent to the fault zone may

**Table 2.**  $Q_D$  Values for the Fault Under Different Reservoir Configurations by Variant Injection Rate and Fracture Spacing Combinations

Injection Rate (kg/s)	Fracture Spacing (m)	$Q_D$
100	1000	$2.6 \times 10^4$
10	1000	$2.6 \times 10^3$
100	100	$2.6 \times 10^2$
50	100	$1.3 \times 10^2$
25	100	$6.5 \times 10^1$
200	10	5.2
100	1	$2.6 \times 10^{-2}$
100	0.1	$2.6 \times 10^{-4}$
100	0.01	$2.6 \times 10^{-6}$

cause seismic fault reactivation, we follow temperature change in the rock using the dimensionless parameters noted earlier. This analysis focuses on predicting the evolution of temperature in the rock (as opposed to fluid temperature as in many prior models [Gringarten *et al.*, 1975; Elsworth, 1990]) and captures the intrinsic relationship between the evolution of dimensionless fault rock temperature  $T_{Dr}$  and dimensionless time

$t_D$  under various dimensionless flow rates  $Q_D$ . Moreover, complementary evaluations of water outflow temperature condition the utility of the reservoir for heat mining where magnitudes of flow rates,  $Q_D$ , are selected to minimize seismic risk.

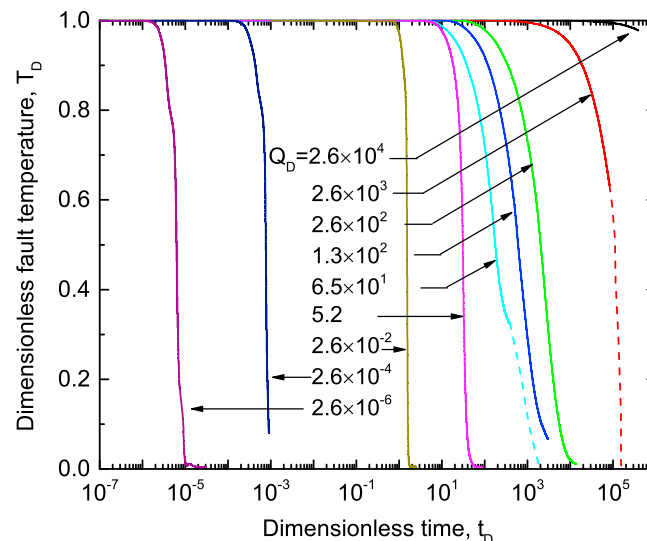
The evolution of dimensionless fault rock temperature  $T_{Dr}$  versus dimensionless time  $t_D/Q_D$  is determined for different dimensionless flow rates  $Q_D$  as shown in Figure 3. This is for fracture network permeability of  $1.0 \times 10^{-13} m^2$  but with different fracture spacing  $s$  to allow the full parameter space of  $Q_D$  to be explored. Apparent is that the thermal drawdown response of the rock is exclusively controlled by the magnitude of  $Q_D$ . Table 2 presents the various  $Q_D$  values under different combinations of injection rate and fracture spacing, respectively. Here the main assumption for the expression of  $Q_D$  is that the direction of heat conduction in the matrix is orthogonal to the direction of the transverse fractures.

Figure 3 shows that the drawdown gradients of dimensionless temperature with time become infinite as represented by a steep (vertical) drawdown response around  $t_D/Q_D \sim 1$ , when the  $Q_D$  value decreases below  $2.6 \times 10^{-4}$ . Solutions are limited to this magnitude due to advection-dominant instabilities in TOUGH (Peclet Number  $> 2.6 \times 10^3$ ) with the dashed line in Figure 3 extrapolating this response. Furthermore, the drawdown response becomes asymptotic to  $t_D/Q_D \sim 1$  as  $Q_D$  approaches  $2.6 \times 10^{-6}$  defining the lower bounding condition where a plug thermal front migrates through the reservoir and consequently yields the highest thermal gradients in space. Conversely, for high  $Q_D$ , the gradient of dimensionless temperature drawdown becomes progressively flatter as the flow rate is increased. When  $Q_D$  reaches  $2.6 \times 10^4$ , the curves become asymptotic to a horizontal line anchored at  $T_D \sim 1$ . This represents the case where water flow through the reservoir is sufficiently rapid that heat transfer from the rock to the fluid

is small. This results in a uniform temperature distribution in the fluid and uniform thermal drawdown in the reservoir.

Thus, the bounding distributions of temperature in the reservoir and how they change with time are conditioned by this non-dimensional flow variable,  $Q_D$ . At high flow rates ( $Q_D > 2.6 \times 10^4$ ) there is little heat transfer from the rock to the water, and the thermal drawdown in the reservoir is uniform as shown in Figure 5. Conversely, when the flow rate is low ( $Q_D < 5.2$ ) then the chilled front in the rock propagates through the reservoir.

An alternate way to represent the transient response of the temperature at the fault within the reservoir by the



**Figure 4.** Dimensionless fault temperature  $T_D$  at the fault vs dimensionless time  $t_D$  under  $Q_D$  varies, respectively, from  $2.6 \times 10^{-6}$  to  $2.6 \times 10^4$ .

dimensionless timing  $t_D$  alone. This dimensionless relationship  $T_D - t_D$  returns a new response of the thermal drawdown in the rock (Figure 4). The individual drawdown curves are parallel for  $Q_D < 5.2$ . The factor  $Q_D$  has an impact in determining the sequence of the parallel curves with a steep decline in time. The curve with the lowest  $Q_D = 2.6 \times 10^{-6}$  indicates the earliest drawdown in dimensionless time as  $t_D = 10^{-5}$ . For this  $Q_D$ -controlled thermal drawdown system, as the  $Q_D$  value grows one order of magnitude when  $Q_D < 5.2$ , the corresponding timing of drawdown is equivalently elevated by one order magnitude. When the  $Q_D > 5.2$ , the gradient of the rock temperature curves decrease gradually as the  $Q_D$  value grows, which represents the case of more significant heat transfer by heat advection. By means of this dimensionless type curve, the timing of thermal drawdown for reservoirs under different configurations may be rigorously explored.

### 5. Thermal Front Propagation and Induced Seismicity

The migration of the thermal front within the reservoir depicts the efficiency of heat recovery from the surrounding geologic medium and controls the form of the thermal gradient at the front. Furthermore, the propagation of the thermal front under different non-dimensional flow rates  $Q_D$  alters the timing of its arrival and therefore the timing of any induced seismicity associated with that thermal stress. Importantly, two bounding behaviors are noted, based on the magnitude of the non-dimensional injection rate,  $Q_D$ . When  $Q_D$  is sufficiently large, the advective heat transfer within the fast flowing fluid is much more efficient than that due to conductive heat transfer to the fluid. In this instance the thermal front propagates from the injection well toward the production well without the presence of distinct uniform thermal front—indeed, in the limit, the water temperature is near uniform throughout the reservoir. Conversely, for small  $Q_D$  the short dimensionless conduction length in the blocks results in more efficient transfer by heat conduction and results in a distinct front but one that displaces at a slower rate  $v_T$ —a velocity  $v_T = \frac{\rho_w c_w}{\rho_r c_r} v_w$ , defined by the product of the ratio of the thermal capacities of water and rock and the fluid velocity  $v_w$  in the fracture.

Figure 5 shows the displacement of the thermal front within the rock as non-dimensional flow rates  $Q_D$  are varied. The injection well is to the left ( $x = 0$  m) with the production well to the right ( $x = 900$  m). The fault is intermediate (dashed arrow) between the injection and production wells. If the  $Q_D$  value is larger than  $2.6 \times 10^2$  (Figure 5c), the rock temperature across the entire reservoir declines uniformly. The flat and uniform drawdown curve corresponds to the larger magnitudes of  $Q_D$  (Figure 5a). Uniform longitudinal thermal drawdown of the rock results in the early breakthrough of cold water (Figure 5a). Conversely, when the  $Q_D$  values are smaller than  $2.6 \times 10^{-2}$ , the thermal front propagates as a thermal shock. Figure 5f with the smallest  $Q_D$  value of  $2.6 \times 10^{-6}$  shows the slowest rate of propagation of the thermal front which identifies the case for the most delayed breakthrough. This represents the case that is most desired in retaining outlet temperatures the highest although flow rates may not be sufficiently high to be economically viable as a geothermal reservoir.

The dimensionless form of timing of the onset of seismicity is linked to the arrival of this front at the location of the fault. This arrival time for the front, traveling a distance  $L^*$  at a propagation velocity  $v_T$  is

$$t_{analytical}^{seismic} = \frac{L^*}{v_T} = \frac{L^*}{\frac{\rho_w c_w}{\rho_r c_r} v_w} = \frac{L^* \rho_r c_r}{v_w \rho_w c_w} \quad (14)$$

Since, the dimensionless time is defined as,

$$t_D = \frac{t}{K_r \rho_r c_r} \left( \frac{q s c_w}{HWL^*} \right)^2.$$

then substituting the dimensional time of equation (2) into equation (3) gives the timing of seismicity as  $t_D \sim Q_D$  (for  $Q_D < 10^0$ ). The relationship between the dimensionless timing for the onset of seismicity and the fluid velocity could be obtained by inserting  $t_{analytical}^{seismic}$  into the equation of dimensionless time,

$$t_D^{seismic} = \frac{L^* \rho_r c_r}{v_w \rho_w c_w} \frac{1}{K_r \rho_r c_r} \left( \frac{q s c_w}{HWL^*} \right)^2 = \frac{L^*}{v_w \rho_w c_w s^2} Q_D^2 \quad (15)$$

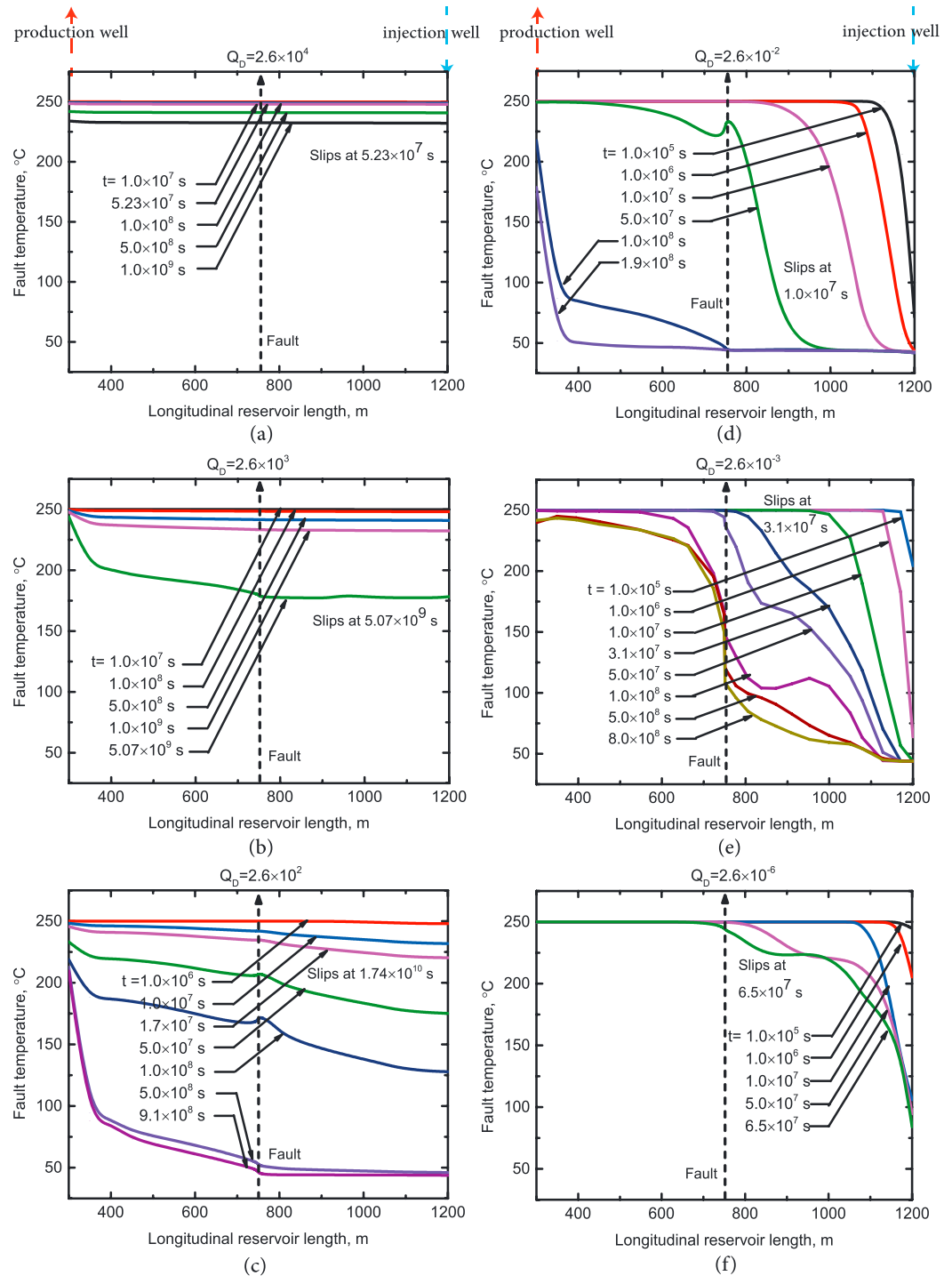


**Figure 5.** Thermal front propagation from the injection well (right axis) toward the production well (left axis) under different  $Q_D$  values; Figures 5a to 5f, respectively, represent the  $Q_D$  values varied from  $2.6 \times 10^4$  to  $2.6 \times 10^{-6}$ .

Therefore, the term  $t_D^{seismic} = \frac{L^* K_r}{v_w \rho_w c_w s^2} Q_D^2$  in equation (15) could be used to capture the dimensionless timing of seismicity. Figure 6 shows that this timing relation is correct for  $Q_D < 5.2$  where the injected fluid is able to completely deplete the heat from the reservoir adjacent to the injection well. When the value of  $Q_D$  is gradually increased above 5.2, then heat transfer by rapid advection dominates over conduction. In this condition there is no distinct thermal front to change the stress state of the fault, and the error in the prediction of timing from this simple relationship  $t_D \sim Q_D$  becomes more significant.

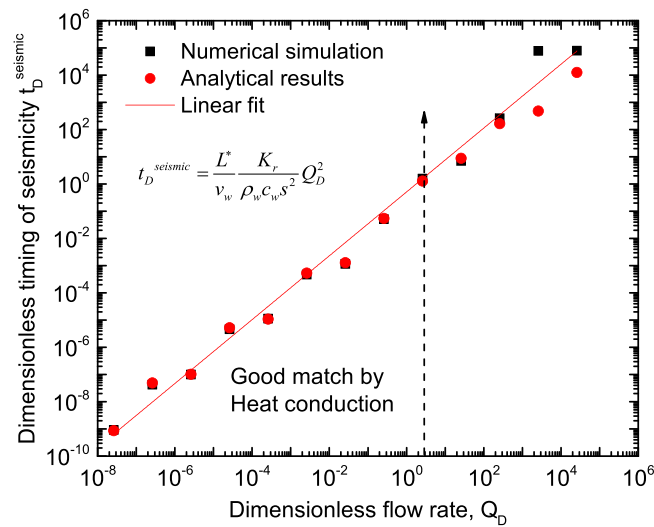


**Figure 6.** Validation of the dimensionless timing equation for the onset of seismicity between numerical simulation results and the analytical results under various  $Q_D$  values ( $Q_D = 2.6 \times 10^{-8} \sim 2.6 \times 10^2$ ). Red circles represent the velocity results from the analytical equation, while the black squares represent the results from the simulations.

From the form of the rate of propagation of the cooling front within the reservoir it is apparent that the non-dimensional timing of arrival of the front scales with dimensionless flow rate (Figure 3). There is a linear relationship implied between  $Q_D$  and the corresponding timing of seismicity  $t_D$  (Figure 6). As the magnitude of  $Q_D$  increases from  $2.6 \times 10^{-6}$ , the dimensionless timing  $t_D$  for the thermally driven induced seismicity increases approximately linearly—enabling timing to be defined in a quantitative manner.

Figure 7 illustrates the thermal evolution of water temperature under the two bounding magnitudes of  $Q_D$  as  $2.6 \times 10^4$  and  $2.6 \times 10^{-3}$ , respectively. At high dimensionless flow rate the cold front reaches the production well after  $1.0 \times 10^7$  s ( $\sim 120$  d). At low dimensionless flow rates ( $Q_D = 2.6 \times 10^{-3}$ ) the outlet

remains at the ambient temperature of the reservoir. This illustrates that geothermal production under large  $Q_D$  values may not be feasible as the advection dominated flow results in premature breakthrough, thus degrading the thermal output for the entire reservoir.

The thermal front propagation under various magnitudes of  $Q_D$  substantially change the evolution of the stress state around the fault. Figure 8 illustrates the thermal evolution of rock temperature under the two bounding magnitudes of  $Q_D$  as  $2.6 \times 10^4$  and  $2.6 \times 10^{-3}$ . This contrasts with Figure 7 for the evolution of water temperature distribution. For  $Q_D = 2.6 \times 10^{-3}$ , the rock and fluid are in thermal equilibrium with no significant temperature difference. A distinct thermal front develops to differentiate the cooled and hot

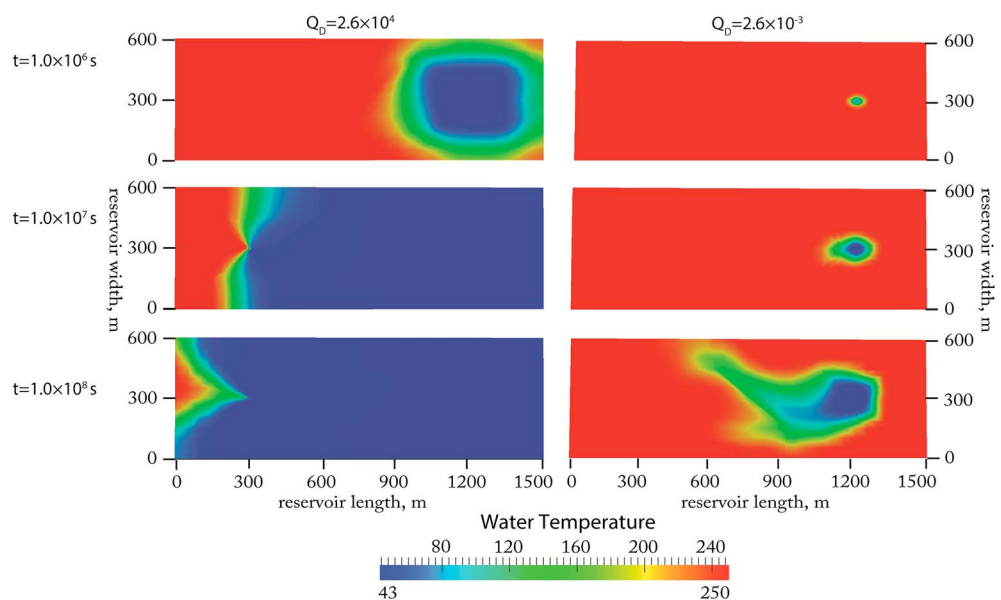


**Figure 7.** Comparison of water temperature evolution in the reservoir under two bounding  $Q_D$  values; the left side figures represent the condition of  $Q_D = 2.6 \times 10^4$ , and the right side figures represent the condition of  $Q_D = 2.6 \times 10^{-3}$ .

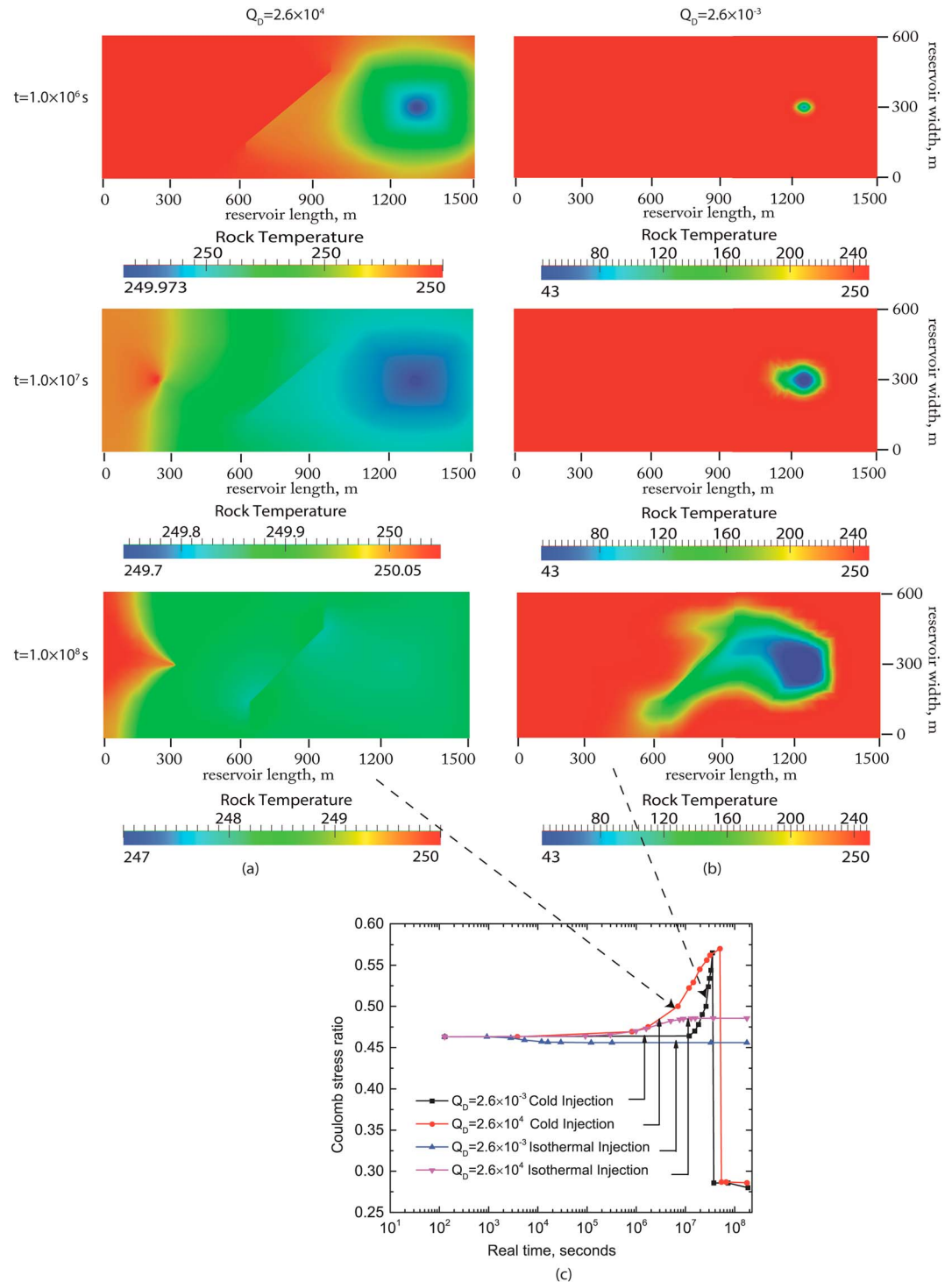


**Figure 8.** Contour of rock temperature distribution at  $t = 1.0 \times 10^6$  s,  $1.0 \times 10^7$  s,  $1.0 \times 10^8$  s, respectively, for (a)  $Q_D = 2.6 \times 10^4$  and (b)  $Q_D = 2.6 \times 10^{-3}$ . Figure 8c represents the evolution of the coulomb stress ratio under  $Q_D = 2.6 \times 10^4$  and  $Q_D = 2.6 \times 10^{-3}$  with isothermal or non-isothermal injection conditions.

region. Conversely, for  $Q_D = 2.6 \times 10^4$  no distinct and observable thermal front develops. Also shown is the evolution of the Coulomb stress ratio ( $\tau/\sigma_{neff}$ ) in Figure 8c. This shows that the stress state of the fault evolves significantly differently due to the bounding styles of thermal propagation in the reservoir at  $Q_D > 2.6 \times 10^4$

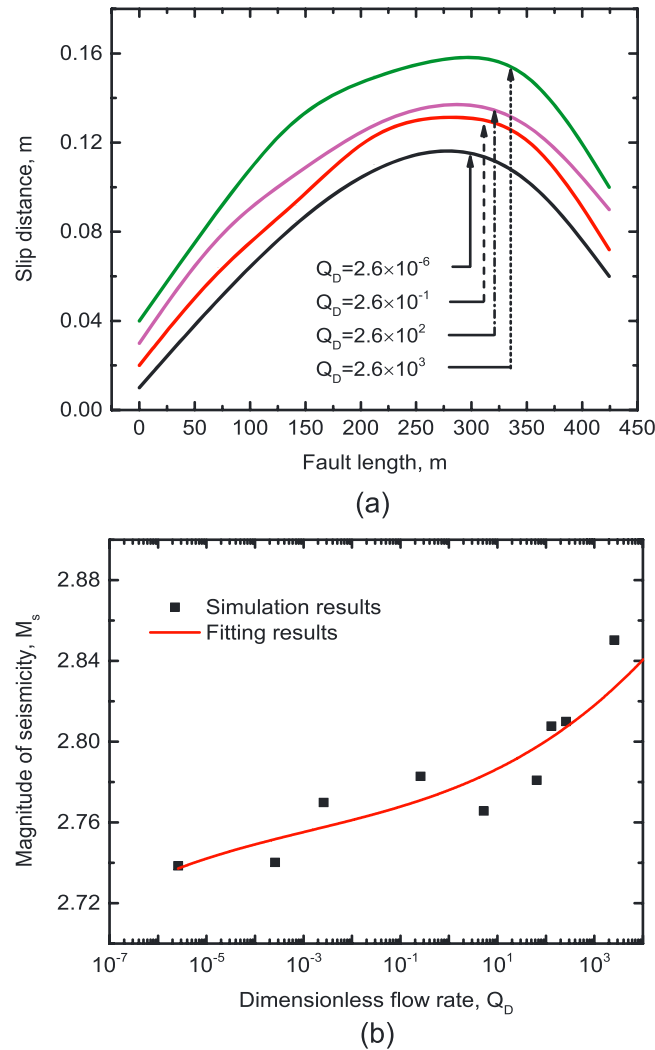


**Figure 9.** (a) The comparison of slip distance distributions in different patches along the fault under the different dimensionless flow rate  $Q_D$ ; (b) the corresponding maximum magnitude of seismicity based on the slip distance results under different flow rate  $Q_D$ .

magnitude of seismicity event also grows. The magnitude of these individual events may be evaluated from the slip distribution as

$$M_0 = \int_0^L \mu L W d D_c \tag{16}$$

where  $M_0$  is seismic moment,  $L$  is the fault length,  $W$  is the width of fault rupture,  $\mu$  is the rigidity of fault (taken here as 1 GPa), and  $D_c$  is the slip distance along the fault patch. This seismic moment may be converted into a moment magnitude  $M_s$ , used to measure the strength of the seismic event. The  $M_s$ - $M_0$  relationship is defined as [Kanamori and Abe, 1979; Purcaru and Berckhemer, 1982],

$$\log M_0 = 1.5 M_s + 16.1. \tag{17}$$

The reservoir thickness is 15 m used in the model. In order to obtain moment magnitudes that are appropriate to the 3-D representation of the fault (fault area of 442 m × 442 m), we use the results from the 2-D plane strain model and extrapolate these over the fault area. This switch between the 2-D slip model and the 3-D fault ignores the clamped boundaries (zero displacement) at the top and base of the fault and would slightly overestimate the moment magnitude—relative to the real case where the edges of the fault are clamped.

and  $Q_D < 2.6 \times 10^{-3}$ . These induced thermal stresses may trigger fault reactivation when the fluid pressures alone are insufficient. We explore this in the following section.

The propagation of the thermal front within the rock is therefore likely an important factor in defining the timing and magnitude of seismicity. When the dimensionless flow rate  $Q_D$  is smaller than  $2.6 \times 10^{-2}$ , the timing of seismicity is exclusively governed by the timing of the arrival of the thermal front at the fault (Figures 5d, 5e, and 5f). In terms of the physical characteristics of the reservoir used here, these correspond to real times of  $t = 1.0 \times 10^7$  s (~100d),  $3.1 \times 10^7$  s (~300d), and  $6.5 \times 10^7$  s (~752d) for  $Q_D = 2.6 \times 10^{-2}$ ,  $2.6 \times 10^{-4}$ , and  $2.6 \times 10^{-6}$ , respectively. Conversely, for large  $Q_D$ , the cooling regime is spread more broadly across the reservoir and therefore may activate a larger patch at this changed stress. Thus, the arrival of the zone of high thermal gradient at the fault is the principal factor that controls the timing of thermally induced seismicity.

Moreover, the slip distance distributions for each patch along the fault reflect the magnitude of the seismic events (Figure 9a) that are associated with the different forms of the migrating thermal front. As the dimensionless injection rate  $Q_D$  increases, the corresponding

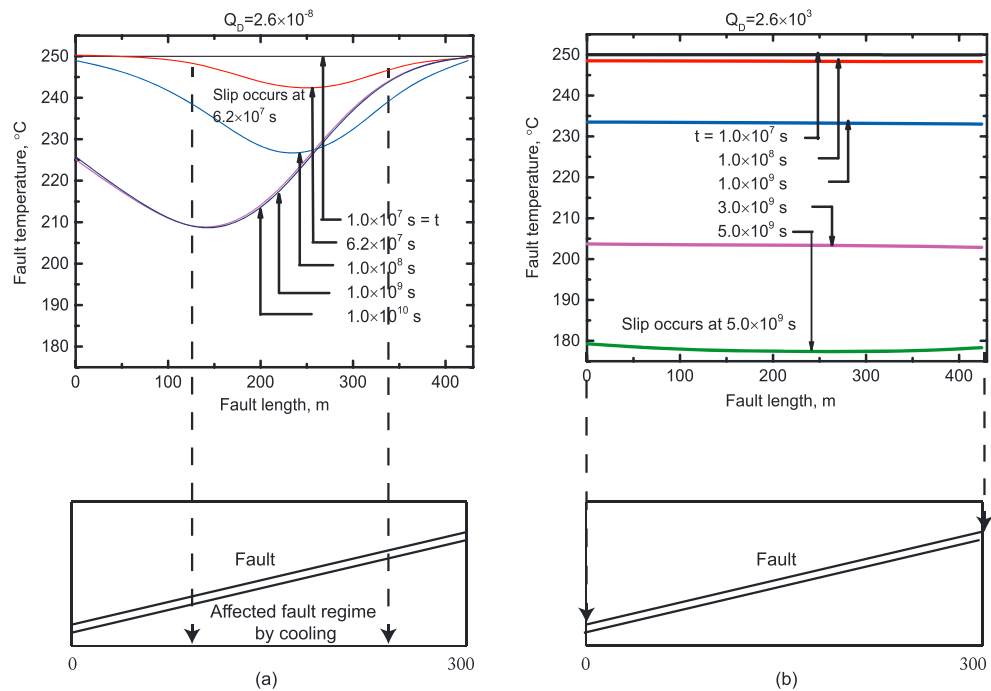


**Figure 10.** (a) The fault temperature evolution under  $Q_D = 2.59 \times 10^{-8}$ . The two dashed lines represent the area affected by the thermal stress acting on the fault when slip occurs at  $6.2 \times 10^7$  s. (b) The fault temperature evolution under  $Q_D = 2.59 \times 10^3$ ; the two dashed lines at the two tips of fault show the fault regime affected by the thermal stress due to the cooling.

Figure 9b indicates that the magnitudes of induced events increase progressively with an increase in the dimensionless flow rate. For small  $Q_D$  ( $2.6 \times 10^{-6}$ ), the resulting event magnitude is 2.74, and this elevates to 2.86 as  $Q_D$  is increased ( $2.6 \times 10^3$ ).

The outcome that the largest circulation rates give the largest events appears to contradict the suggestion that the largest events will result from the most non uniform thermal field—a thermal field that will occur for the lowest flow rates. A plausible mechanism for this observation is that the chilled area along the fault, which ultimately contributes to the destressing and then slips, correlates positively with  $Q_D$ . Thus, the larger flow rates result in a larger cooled region on the fault, and although the stress drops are smaller than for the abrupt thermal front, the resulting product of stress drop and slipped area are larger. Figure 10a ( $Q_D = 2.6 \times 10^{-8}$ ) shows that only a small portion of the fault is locally affected by the arrival of the thermal front for small non-dimensional flow rates ( $t = 6.2 \times 10^7$  s). In comparison, for a larger  $Q_D$  ( $2.6 \times 10^3$ ; Figure 10b), the cumulative thermal stress initiates a larger fault reactivation at later time ( $t = 5.0 \times 10^9$  s) since the entire fault is uniformly cooled. This explains the observations of Figure 9 where event magnitude grows with  $Q_D$ . Thus, both the dimensionless timing of seismicity  $t_D$  and the event magnitude  $M_s$  both increase with an increase in the dimensionless flow rate as shown in Figures 9 and 10.

### 6. Output Power Optimization

Since the propagation of the thermal front at different dimensionless flow rates  $Q_D$  influences both the form and distribution of thermal drawdown within the reservoir, the overall thermal output of the reservoir should scale with  $Q_D$ . Thus, the rate of thermal energy production (power) may be determined scaled with this parameter, together with its longevity. These two observations together give the cumulative energy output.

Thermal power output,  $P_t$ , may be defined as,

$$P_t = Q\Delta H \tag{18}$$

where  $Q$  is the mass flow rate (kg/s), and  $\Delta H$  is the enthalpy difference between the outlet water enthalpy and the enthalpy of injection water.

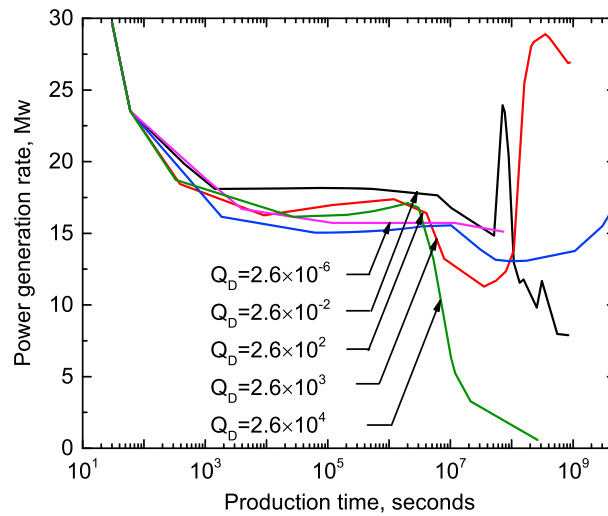


**Figure 11.** The results of power generation rate calculation under different  $Q_D$  values within 50 years injection. The magenta curve represents the smallest  $Q_D$   $2.6 \times 10^{-6}$ , and the green curve represents the largest  $Q_D$  value equal to  $2.59 \times 10^4$ .

Figure 11 compares the evolution of power generation rate for various  $Q_D$ . The curves share an identical initial generation rate of  $\sim 30$  MW, but diverge after the transient production period  $t = 1.0 \times 10^3$  s. The response for the two end-member magnitudes of  $Q_D$  ( $2.6 \times 10^{-6}$  and  $2.6 \times 10^4$ ) represent the two most unfavorable production scenarios. At large flow rates ( $Q_D > 2.6 \times 10^4$ ) the reservoir is unable to transfer heat to the massive flux of cold water after the initial removal of heat from the fracture skin. As a consequence the outlet drops precipitously after  $t = 1.0 \times 10^7$  s ( $\sim 115$  d). The converse is true at low flow rates ( $Q_D = 2.6 \times 10^{-6}$ ) where the output is hot but the low mass flow rate limits power generation to  $\sim 15$  Mw. The

sweetspot with the most favorable conditions for power generation are in the range  $Q_D = 2.6 \times 10^{-2} \sim 2.6 \times 10^2$ . The curve with  $Q_D = 2.6 \times 10^{-2}$  yields the maximum cumulative power generation within 1 year, while the red curve with  $Q_D = 2.6 \times 10^2$  results in larger potential of late stage power generation. It could be explained that the large volume of injection reduced the effective stress by elevating the pore pressure of reservoir at a large extent; the permeability around the production well could be further improved by the occurrence of fracture shearing. Therefore, the mass flow rate at the outlet increased significantly. According to Figure 11, it is desirable to produce the geothermal reservoir with flow rates in the range  $Q_D = 2.6 \times 10^{-2} \sim 2.6 \times 10^2$  to maximize energy recovery.

## 7. Conclusions

The foregoing defines the evolution of heat transfer in a fractured geothermal reservoir characterized by non-dimensional parameters. The evolution of water temperature and mean temperature in the rock is conditioned by dimensionless parameters representing the flow rate  $Q_D$  and time  $t_D$ . The dimensionless flow rate  $Q_D$  is conditioned by the in situ fracture spacing, prescribed mass injection rate, and reservoir geometry and influences the thermal drawdown response of the reservoir. The sensitivity tests have explored the effect of, fracture spacing, fault permeability, and injection temperature [Gan and Elsworth, 2014]. Based on this dimensionless model, this work captures the thermal drawdown response of the host hot rock at different reservoir scales and for different spacing and permeabilities of fracture networks. More importantly, the timing and magnitude of thermally driven fault seismicity are rigorously investigated under the various scenarios of thermal front propagation in rocks.

The primary control parameter  $Q_D$  transforms dimensionless timing and temperature data into two bounding asymptotic behaviors. These two bounding asymptotic behaviors refer to the situations of heat transfer dominated by heat conduction where the drawdown gradients of dimensionless temperatures with time become asymptotically and infinitely steep (vertical) around  $t_D/Q_D \sim 1$ , when the  $Q_D$  value decreases below  $2.6 \times 10^{-4}$ . When  $Q_D$  reaches  $2.6 \times 10^4$ , the curves become asymptotic to a horizontal line anchored at  $T_D \sim 1$ . This represents the case where the velocity of fluid in the reservoir is sufficiently rapid that heat transfer from the rock to the fluid is conduction limited and small. This results in an early cold water breakthrough at the outlet and uniform thermal drawdown in the rock. The magnitude of  $Q_D$  has an impact in determining the sequence of the parallel steep curves (dimensionless  $t_D$ ). When the  $Q_D$  value grows by one order of magnitude, the corresponding dimensionless timing  $t_D$  for thermal depletion of water or rock is approximately elevated by one order magnitude for  $Q_D < 5.2$ . The situation with a lower magnitude  $Q_D$  ( $< 5.2$  in this model configuration) yields a uniform propagation of the thermal front, while

the case with larger magnitude  $Q_D$  ( $> 2.6 \times 10^2$ ) produces a more uniform thermal distribution across the whole reservoir without a distinct thermal front.

Under the condition of propagation of a uniform thermal front, the timing for fault reactivation is determined as the thermal front arrives at the fault. The spatial thermal gradient adjacent to the front (and then arriving at the fault) is the principal factor defining the timing of triggered seismicity. As the dimensionless ratio  $Q_D$  increases, accordingly the dimensionless timing for the onset of thermal-driven seismicity is also linearly increased. Similarly, the magnitude of fault slip distance also grows with increments in  $Q_D$ , since the cooled area of fault area that exhibits thermal stress changes is proportionally increased with an increase in  $Q_D$ .

Finally, the  $Q_D$  magnitude plays an important role in determining the rate of power generation and the ultimate heat extraction efficiency of the reservoir. It reveals that the optimum water production condition is located at an intermediate magnitude of  $Q_D$  in the range of  $2.6 \times 10^{-2} - 2.6 \times 10^2$ . The two bounding magnitudes of  $Q_D$  represent unfavorable conditions where flow rates are either too small or outlet temperatures too small to yield significant power.

#### Acknowledgments

Data supporting Figures 3–6 and 8–11 are available as in Supporting Information Datasheet for Figures 3–11. xlsx S1. This work is the result of partial support from the US Department of Energy under project DOE-DE-343 EE0002761. This support is gratefully acknowledged. The authors would like to thank the anonymous reviewers for their valuable comments and suggestions to improve the quality of the paper.

#### References

- Biot, M. A. (1941), General theory of three-dimensional consolidation, *J. Appl. Phys.*, *12*(2), 155–164.
- Bodvarsson, G. (1969), On the temperature of water flowing through fractures, *J. Geophys. Res.*, *74*(8), 1987–1992, doi:10.1029/JB074i008p01987.
- Bödvarsson, G. S., and C. F. Tsang (1982), Injection and Thermal Breakthrough in Fractured Geothermal Reservoirs, *J. Geophys. Res.*, *87*(B2), 1031–1048, doi:10.1029/JB087iB02p01031.
- Byerlee, J. (1978), Friction of rocks, *Pure Appl. Geophys.*, *116*(4–5), 615–626.
- Elsworth, D. (1989a), Thermal recovery from a multiple stimulated HDR reservoir, *Geothermics*, *18*(5–6), 761–774.
- Elsworth, D. (1989b), Theory of thermal recovery from a spherically stimulated hot dry rock reservoir, *J. Geophys. Res.*, *94*(B2), 1927–1934, doi:10.1029/JB094iB02p01927.
- Elsworth, D. (1990), A comparative evaluation of the parallel flow and spherical reservoir models of HDR geothermal systems, *J. Volcanol. Geotherm. Res.*, *44*(3–4), 283–293.
- Elsworth, D., and J. Xiang (1989), A reduced degree of freedom model for permeability enhancement in blocky rock, *Geothermics*, *18*(5/6), 691–709.
- Gan, Q., and D. Elsworth (2014), Analysis of fluid injection-induced fault reactivation and seismic slip in geothermal reservoirs, *J. Geophys. Res. Solid Earth*, *119*, 3340–3353, doi:10.1002/2013JB010679.
- Ganguly, S., and M. S. Mohan Kumar (2014), Analytical solutions for transient temperature distribution in a geothermal reservoir due to cold water injection, *Hydrogeol. J.*, *22*(2), 351–369.
- Ghassemi, A., S. Tarasovs, and A. H.-D. Cheng (2003), An integral equation solution for three-dimensional heat extraction from planar fracture in hot dry rock, *Int. J. Numer. Anal. Methods Geomech.*, *27*(12), 989–1004.
- Gringarten, A. C., and P. A. Witherspoon (1973), Extraction of heat from multiple-fractured dry hot rock, *Geothermics*, *2*(3–4), 119–122.
- Gringarten, A. C., P. A. Witherspoon, and Y. Ohnishi (1975), Theory of heat extraction from fractured hot dry rock, *J. Geophys. Res.*, *80*(8), 1120–1124, doi:10.1029/JB080i008p01120.
- Holman, J. P. (2002), *Heat Transfer*, 9th ed., McGraw Hill, New York.
- Kanamori, H., and K. Abe (1979), Reevaluation of the turn-of-the-century seismicity peak, *J. Geophys. Res.*, *84*(B11), 6131–6139, doi:10.1029/JB084iB11p06131.
- Pruess, K. (1983), Heat transfer in fractured geothermal reservoirs with boiling, *Water Resour. Res.*, *19*(1), 201–208, doi:10.1029/WR019i001p0201.
- Pruess, K., and Y.-S. Wu (1993), A new semi-analytical method for numerical simulation of fluid and heat flow in fractured reservoirs, *SPE Adv. Technol. Ser.*, *1*(02), 63–72.
- Purcaru, G., and H. Berckhemer (1982), Quantitative relations of seismic source parameters and a classification of earthquakes, *Tectonophysics*, *84*(1), 57–128.
- Segall, P., S. D. Fitzgerald (1998), A note on induced stress changes in hydrocarbon and geothermal reservoirs, *Tectonophysics*, *289*(1–3), 117–128, ISSN: 0040-1951, doi:10.1016/S0040-1951(97)00311-9.
- Shaik, A. R., S. S. Rahman, N. H. Tran, and T. Tran (2011), Numerical simulation of Fluid-Rock coupling heat transfer in naturally fractured geothermal system, *Appl. Therm. Eng.*, *31*(10), 1600–1606.
- Taron, J., and D. Elsworth (2009), Thermal–hydrologic–mechanical–chemical processes in the evolution of engineered geothermal reservoirs, *Int. J. Rock Mech. Min. Sci.*, *46*(5), 855–864.
- Taron, J., and D. Elsworth (2010), Coupled mechanical and chemical processes in engineered geothermal reservoirs with dynamic permeability, *Int. J. Rock Mech. Min. Sci.*, *47*(8), 1339–1348.
- Xu, T., E. Sonnenthal, N. Spycher, K. Pruess, G. Brimhall, and J. Apps (2001), Modeling multiphase non-isothermal fluid flow and reactive geochemical transport in variably saturated fractured rocks: 2. Applications to supergene copper enrichment and hydrothermal flows, *Am. J. Sci.*, *301*(1), 34–59.
- Xu, T., J. A. Apps, and K. Pruess (2003), Reactive geochemical transport simulation to study mineral trapping for CO<sub>2</sub> disposal in deep arenaceous formations, *J. Geophys. Res.*, *108*(B2), 2071, doi:10.1029/2002JB001979.
- Xu, T., E. Sonnenthal, N. Spycher, and K. Pruess (2004), TOUGHREACT user's guide: A simulation program for non-isothermal multiphase reactive geochemical transport in variably saturated geologic media, *Rep. LBNL-55460*, Lawrence Berkeley Natl. Lab., Univ. of Calif., Berkeley.